8. G. Kresse, J. Furthmüller, *Phys. Rev. B* **54**, 11169 (1996).
9. V. Milman *et al.*, *Int. J. Quantum Chem.* **77**, 895 (2000).
10. P. Blaha, K. Schwarz, G. Madsen, D. Kvasnicka, J. Luitz, *WIEN2k, An Augmented Plane Wave + Local Orbitals Program for Calculating Crystal Properties* (Technische Universität Wien, Vienna, 2001).
11. The ABINIT code is a common project of the Université Catholique de Louvain (Louvain-la-Neuve, Belgium), Corning Incorporated (Corning, NY), and other contributors (available at www.abinit.org).
12. J. P. Perdew *et al.*, *Phys. Rev. B* **46**, 6671 (1992).
13. M. Methfessel, A. T. Paxton, *Phys. Rev. B* **40**, 3616 (1989).
14. J. P. Perdew, K. Burke, M. Ernzerhof, *Phys. Rev. Lett.* **77**, 3865 (1996).
15. N. Troullier, J. L. Martins, *Phys. Rev. B* **43**, 1993 (1991).
16. G. Kresse, D. Joubert, *Phys. Rev. B* **59**, 1758 (1999).
17. For verification, the input files for the different codes are maintained at a publicly accessible Web site (available at http://asm.mit.edu/sogata/AlCu/).
18. C. R. Krenn, D. Roundy, J. W. Morris Jr., M. L. Cohen, *Mater. Sci. Eng. A* **317**, 44 (2001).
19. J. Li, K. J. Van Vliet, T. Zhu, S. Yip, S. Suresh, *Nature* **418**, 307 (2002).
20. P. J. Feibelman, *Phys. Rev. Lett.* **65**, 729 (1990).
21. J. C. Grossman, A. Mizel, M. Côté, M. L. Cohen, S. G. Louie, *Phys. Rev. B* **60**, 6343 (1999).
22. N. Kioussis, M. Herbranson, E. Collins, M. E. Eberhart, *Phys. Rev. Lett.* **88**, 125501 (2002).
23. Y. Umeno, T. Kitamura, *Mater. Sci. Eng. B* **88**, 79 (2002).
24. Y. Mishin, M. J. Mehl, D. A. Papaconstantopoulos, A. F. Voter, J. D. Kress, *Phys. Rev. B* **63**, 224106 (2001).
25. Landolt-Börnstein III/14a, *Structure Data of Elements and Intermetallic Phases. Elements, Borides, Carbides, Hybrides*, K.-H. Hellwege, A. M. Hellwege, Eds. (Springer-Verlag, New York, 1988).
26. C. Stampfl, C. G. Van de Walle, *Phys. Rev. B* **59**, 5521 (1999).
27. F. Jona, P. M. Marcus, *Phys. Rev. B* **63**, 094113 (2001).
28. Landolt-Börnstein III/29a, *Low Frequency Properties of Dielectric Crystals Second and Higher Order Elastic Constants*, D. F. Nelson, Ed. (Springer-Verlag, New York, 1992).
29. J. P. Hirth, J. Lothe, *Theory of Dislocations* (Wiley, New York, ed. 2, 1982).
30. J. Hartford, B. von Sydow, G. Wahnström, B. I. Lundqvist, *Phys. Rev. B* **58**, 2487 (1998).
31. G. Lu, N. Kioussis, V. V. Bulatov, E. Kaxiras, *Phys. Rev. B* **62**, 3099 (2000).
32. We thank J. W. Morris Jr. for comments on the manuscript. S.O. thanks Y. Shibutani and H. Kitagawa for discussions and acknowledges support by a Murata-Kaigai-Ryugaku-Syogakukai fellowship. J.L. and S.Y. acknowledge support by Honda R&D; the Air Force Office of Scientific Research; NSFKDI and ITR initiatives; and Lawrence Livermore National Laboratory.

26 July 2002; accepted 11 September 2002

The Effect of Size-Dependent Nanoparticle Energetics on Catalyst Sintering

Charles T. Campbell, Stephen C. Parker, David E. Starr

Calorimetric measurements of metal adsorption energies directly provide the energies of metal atoms in supported metal nanoparticles. As the metal coverage increases, the particles grow, revealing the dependence of this energy on particle size, which is found to be much stronger than predicted with the usual Gibbs-Thompson relation. It is shown that this knowledge is crucial to accurately model long-term sintering rates of metal nanoparticles in catalysts.

Metal nanoclusters, dispersed across the surface of an oxide or other support, can be much more active and selective as catalysts than can larger metal particles (*1*, *2*). However, metal nanoclusters invariably sinter (form larger clusters) under reaction conditions, especially in some very important technical catalysts (*2*–*8*). The development of supported metal nanoclusters that resist long-term sintering has been hampered by the lack of a kinetic model that accurately predicts long-term sintering based on short-term measurements. Without such a model, every promising new catalyst must be tested for the actual length of time it must resist sintering in application (~1 year).

We show here that the inclusion of accurate size dependence of particle energies in kinetic models is crucial in this respect. Little is currently known experimentally about the energetics of atoms within metal nanoparticles, although the energy of gaseous Sn clusters as a function of size was measured recently (*9*), and theoretical calculations continue to address this important issue (*10*, *11*). The direct determination of particle energies via calorimetry has been developed relatively recently. In addition, the roughness of real catalyst supports can make it difficult to determine particle sizes via microscopic methods as a function of temperature. In the absence of direct measurements, a commonly used approach for estimating the dependence of particle energy on size has been to use the Gibbs-Thompson relation, which states that the chemical potential (partial molar free energy) of a metal atom in a particle of radius R, $\mu(R)$, differs from that in the bulk [$\mu(\infty)$] by

$$\mu(R) - \mu(\infty) = 2\gamma\Omega/R \qquad (1)$$

where γ is the surface free energy of the metal and Ω is the bulk metals volume per atom (*4*, *12*). The use of this relation is implicit in all current atomistic models of sintering (*13*–*15*), starting with the pioneering models of Wynblatt and Gjostein (W-J) (*3*, *4*).

In this report, we use our recent microcalorimetric measurements of the heat of adsorption (q_{ad}) of Pb onto MgO(100) (*16*) to show that the energy of a metal atom in a nanoparticle increases much more dramatically with decreasing size than predicted by the Gibbs-Thompson relation. Because the Pb immediately forms Pb nanoparticles upon adsorption, and these grow in radius smoothly with increasing coverage, this measured adsorption energy versus coverage directly provides the difference in energy between gaseous Pb and a Pb atom in a nanoparticle as a detailed function of particle size (Fig. 1). We then develop a model for predicting particle size evolution based on modified bond additivity that better approximates the calorimetric data. Kinetic models of sintering rates based on our modified bond-additivity estimate are compared to the W-J model, as well as to heuristic models that have been developed because of the inaccuracies of the W-J model. We use our modified bond-additivity model to predict the sintering of gold particles on TiO_2 and compare these model results to experimental data we obtained via temperature-programmed low-energy ion scattering (TP-LEIS).

We can convert our calorimetric data for Pb on MgO(100) (*16*) to energy versus particle size, because there is good evidence that Pb grows on this surface as nearly hemispherical particles with roughly constant number density of $\sim 8.1 \times 10^{11}$ islands/cm^2, after the first few percent of a monolayer. Using this particle density, the measured Pb surface concentration can be converted directly into the average number of atoms per particle, and then into the average hemispherical particle radius (Fig. 1). As can be seen, the stability of the metal atoms in a Pb particle (that is, their heat of adsorption, relative to gaseous Pb) decreases dramatically as the radius decreases below a few nanometers (*17*). For comparison to these direct measurements of the effect of the metal particle size on the metal atom's energy, the predictions of the Gibbs-Thompson relation [Eq. 1, taking $\gamma = 58.6$ μJ/cm^2 for Pb (*18*)] are also plotted in Fig. 1 as "constant γ model". Here, we neglect entropy differences (*12*), so that $q_{ad}(R) - q_{ad}(\infty) = -[\mu(R) - \mu(\infty)] = -2\gamma\Omega/R$, where $q_{ad}(R)$ is the differential molar heat of adsorption of Pb at fixed radius R. As is seen, Eq. 1 severely overpredicts the stability of Pb in small Pb particles, by ~60 kJ/mol at 1 nm radius (*19*). This shows that the surface energy increases substantially as the radius decreases below ~3 nm, which could be ex-

Department of Chemistry, Box 351700, University of Washington, Seattle, WA 98195–1700, USA.

pected because the average coordination number of the surface atoms decreases. This is the same reason why more open or stepped crystal facets of metals have higher surface energies (*20*). An often-cited derivation for liquid metal droplets (*21*), also extended to solid particles (*22*), predicts that surface energy decreases with decreasing radius, which is opposite to our data.

A simple, modified, pairwise bond-additivity (MBA) model reproduces the dramatic dependence of energy on cluster size surprisingly well near a radius of 0.5 to 2 nm, relative to infinite radius (Fig. 1). In this model, the energies of discrete compact clusters were calculated, assuming that all metal-metal bond energies equal their bulk value [32.5 kJ/mol, or 1/6 of the sublimation energy of bulk solid Pb, 195.2 kJ/mol (*23*)]. Very stable cluster shapes were chosen by adding successive hexagonal close-packed layers, with the number of atoms in each layer starting from the top given by 1, 3, 7, 12, . . . (that is, each new underlayer providing a threefold hollow site for each atom in the layer above). The effective radius R of each such cluster was calculated from its volume (V), assuming hemispherical shape, as follows: V = the number of atoms in a cluster times $\Omega = 2\pi R^3/3$. The energies for other cluster sizes were assumed to vary linearly with radius between these compact clusters, thus modifying true bond additivity.

There are two compensating errors in this MBA model. First, metal-metal bond energies actually increase as the coordination number (CN) of the metal atoms involved decreases (*10*, *24*). Second, MBA interpolates linearly between points calculated only for the most compact clusters, whereas atoms in most small clusters are actually less stable because of their lower average CN. Because these errors roughly compensate for one another, there is reasonable agreement with the data. This justifies the use of this MBA model with other face-centered cubic (fcc) metals for which the calorimetry data are not yet available (as we do below for gold), at least for qualitative understanding of the effect of their particle size on energy. We do this by scaling the island energies found for Pb (Fig. 1) by their metal-metal bond strength (or bulk sublimation energy), and their effective radii by $\Omega^{1/3}$, both relative to the values for Pb. Extrapolating to other fcc metals in this way is quite reasonable, at least for the noble and late transition metals, given the similarity found by DePristo (*10*) between all of these fcc metals and Pb in the relation between energy and CN (*25*).

Sintering of supported metal catalysts is often modeled in terms of "Ostwald ripening," in which individual metal atoms (possibly in the form of a complex with another species, hence "monomers") leave a metal cluster, diffuse over the support, and join another metal cluster (*3*–*5*, *7*, *8*, *13*, *14*, *26*). Energetics favor the formation of larger clusters. Models of sintering based on this same atomic-level mechanism were developed early by W-J (*3*, *4*). In their "interface-controlled" Ostwald ripening model, based on classical nucleation theory (*3*, *4*), the rate of change of a metal particle's radius (R) is given by

$$dR/dt = (K/R)(e^{-E_{tot}/kT})[e^{\{\mu(R^*)-\mu(\infty)\}/kT} - e^{\{\mu(R)-\mu(\infty)\}/kT}] \quad (2)$$

where E_{tot} is the metal's bulk sublimation enthalpy (ΔH_{sub}) minus the adsorption energy of a monomer on the support ($E_{ad}^{support}$), plus the diffusion activation energy of a metal monomer atom on the support ($E_{diff}^{support}$); k is Boltzmann's constant; T is the temperature of the substrate; $R^* = 1/(\text{average of } 1/R \text{ for all particles})$; and $K = [(2 \sin\theta)(\nu_P)(\Omega)]/[(2 - 3\cos\theta + \cos^3\theta)(a)]$, where θ is the equilibrium contact angle of the metal particles with the support surface, ν_P is the prefactor in the rate constant for the elementary step wherein a metal monomer diffusing along the edge of a particle leaves that particle to move out onto the support surface, and a is the interatomic spacing in the metal (*27*).

W-J simplified Eq. 2 to

$$dR/dt = [2\gamma\Omega K/(kTR^2)](e^{-E_{tot}/kT})[R/R^* - 1] \quad (3)$$

by substituting the Gibbs-Thompson relation (Eq. 1) for $\mu(R) - \mu(\infty)$. We showed above that this assumption has errors of ~60 kJ/mol for 2-nm diameter particles relative to large particles. Given that this error is in the exponent of Eq. 2, Eq. 3 would be in error by many orders of magnitude when modeling long-term sintering wherein the particles increase in size across the whole range of Fig. 1. Equation 3 predicts that large particles sinter much more rapidly than they really do when the data are fit to short-term (small-particle) kinetics to get the apparent activation energy (*28*).

Figure 2 highlights the difference in the predicted sintering kinetics for Pb particles on MgO(100), using Eq. 2 with two different models for the particle energetics: Eq. 1 and the MBA model. The fraction of an MgO(100) surface covered by Pb particles (a measure of the particle dispersion) is plotted versus temperature as the Pb/MgO(100) surface is heated with a linear heating ramp (1.0 K/s) from 250 to 700 K. Following kinetics during such a heating ramp is a quick way to probe the broad range of apparent activation energies for sintering that arise from its strong size dependence. The starting surface was assumed to have Pb islands with a Gaussian distribution of radii, with average radius of 0.6 nm and a full width at half maximum (FWHM) of 0.2 nm. These simulations were done by numerically propagating island radii with time according to Eq. 2, using finite difference methods. In both simulations shown, parameters appropriate for Pb/MgO(100) were used: E_{tot} = 141 kJ/mol, $\theta = 90°$, and $\nu_P = 3 \times 10^{12}\ s^{-1}$ (*16*, *29*). In one simulation, the metal atom chemical potential versus radius was calculated with Eq. 1, assuming that the surface energy of all Pb particles equals the bulk value for solid Pb [58.6 μJ/cm² (*18*)], as in Eq. 3. In the other

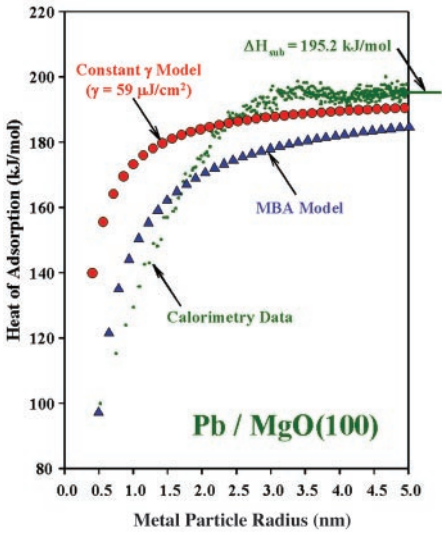

Fig. 1. Measured differential heat of adsorption versus coverage of Pb onto MgO(100) from (*16*), replotted as a function of the average Pb particle radius, to which the Pb atom adds upon adsorption. For comparison, also shown are the results predicted by Eq. 1 assuming that the surface energy is constant at its value for bulk solid Pb [59 μJ/cm² (*18*)], and by an MBA model.

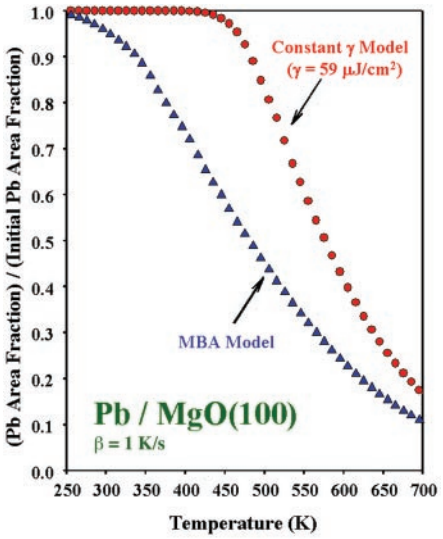

Fig. 2. Simulations of sintering kinetics using Eq. 2 with parameters appropriate for Pb/MgO(100). One curve assumes that the surface energy is fixed at its bulk value, whereas the other curve uses the strong dependence of surface energy on particle radius of the MBA model, similar to that measured calorimetrically (Fig. 1).

simulation, the chemical potential versus radius was calculated with the MBA model of Fig. 1, which is a much closer approximation to the real measured energy. As can be seen, the sintering extends over a much broader temperature range in this more accurate model—a range that is twice as wide in absolute temperature. This broad temperature range is required because of the dramatic change in energy with particle radius (Fig. 1).

The inability of the W-J model of Eq. 3 to reproduce the rapid decrease in sintering rate seen experimentally at fixed temperature has been noted in the past. A "generalized power law" is more commonly used now to model sintering kinetics (*6*, *7*, *30*), although it has no underlying atomistic mechanism but artificially incorporates an equilibrium level of sintering (*6*, *7*, *30*, *31*).

The accuracy of Eq. 2 in simulating measured sintering kinetics, when combined with the MBA model to estimate particle energetics, is demonstrated next for the case of Au particles on the TiO_2(110) surface (Fig. 3). This system has been widely studied as a model of Au nanoparticle catalysts (*1*, *32*, *33*), which are active in low-temperature CO oxidation and selective oxidations (*2*). We followed the sintering of the Au particles via TP-LEIS, using the ultrahigh-vacuum equipment described in (*32*, *34*). The catalyst was heated at a constant rate ($\sim$1 K s^{-1}), and the LEIS peak intensities for both the metal and the substrate oxide were measured every $\sim$1 s (Fig. 3). This method directly measures the fraction of the surface covered by metal islands, which is the same measure of metal dispersion as in Fig. 2. This technique has the advantage that it probes, in a single fast experiment, the very broad range of

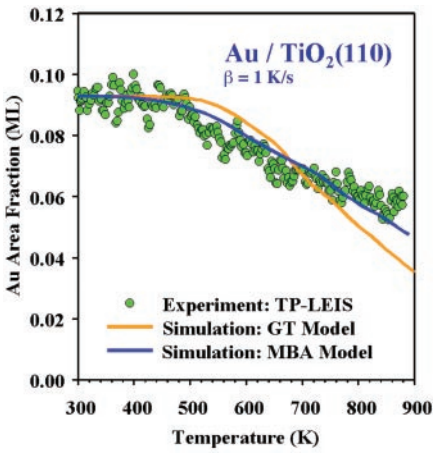

Fig. 3. Thermal sintering kinetics of Au islands on TiO_2(110), as measured by TP-LEIS. The fraction of the surface covered by Au islands was directly measured by the intensity of the Au-LEIS peak normalized by its value for pure Au multilayers. Heating rate = 1 K s^{-1}. Also shown are simulations of Eq. 2, with the particle energetics estimated using the MBA model and, for comparison, the Gibbs-Thompson (GT) relation.

effective activation energies involved in sintering particles from 1 to 10 nm in diameter as revealed above (sampled instead with industrial catalysts by running for years at lower temperature). Probing this full activation energy range is essential for a complete understanding of the mechanism and microkinetic parameters involved, which must underlie any long-term predictive models of catalyst sintering. The results show that Au sintering begins at $\sim$400 K but requires >900 K (at 1 K s^{-1}) for completion. This result is surprising, because even at 140 K, Au atoms can easily migrate across Au-free patches of the oxide surface and up onto the tops of three-dimensional Au islands (*34*). Our simulations described below show that sintering is not complete even by 900 K because of the dramatic effect of particle size on chemical potential (and effective activation energy) of the type demonstrated in Fig. 1

Figure 3 also shows our numerical simulations of these data, using Eq. 2 together with the MBA model above to estimate the effect of Au particle radius on the energy (μ) of Au atoms in these particles. No calorimetric data are available for Au, so we used this model to estimate the difference in energy between tiny particles (with radii of 0.5 to 4 nm) and infinite radius. The fit of Eq. 2 to the Au/TiO_2(110) data is quite good in that the very broad range of temperatures is well reproduced. The adjustable parameters used in this model were all physically reasonable: E_{tot} = 327 kJ/mol, θ = 90°, and $\nu_P = 4 \times 10^{12}$ s^{-1}. [Large Au clusters on TiO_2(110) were estimated to have an equilibrium contact angle of 120° (*33*), but small clusters should have a smaller contact angle (*35*, *36*).] The initial islands were assumed to have a Gaussian radius distribution with an average of 0.5 nm and FWHM of 0.2 nm (*37*). Because ΔH_{sub} for Au is 368 kJ/mol (*23*), the best-fit value of E_{tot} (327 kJ/mol) implies that $E_{ad}^{support} - E_{diff}^{support}$ is 41 kJ/mol, which is also quite reasonable given that $E_{ad}^{support}$ for Au on alumina was estimated to be $\sim$30 kJ/mol by modeling of nucleation kinetics (*38*). [On TiO_2, $E_{ad}^{support}$ could easily be larger because of the different material and/or its larger density of surface defects (*34*). Although defects are not explicitly considered in the W-J model, they would effectively increase $E_{ad}^{support}$ (*8*, *34*).] The influence of variations in these parameters on sintering are described in (*39*).

For comparison to the simulation of Eq. 2 using the MBA model, Fig. 3 also shows its simulation with all the same parameters but using the Gibbs-Thompson relation instead for particle energies [with γ = 140 μJ/cm^2 for Au (*40*)], adjusting E_{tot} to 265 kJ/mol to fit the data. This model predicts that sintering starts too high in temperature and finishes too soon. It implies that $E_{ad}^{support} - E_{diff}^{support}$ is 103 kJ/mol, which is unreasonably high.

In spite of decades of research in developing sintering kinetic models (*3*–*7*, *30*), no atomistic models reproduced the very high temperatures and broad temperature range over which the observed sintering occurs. Our model reproduces and qualitatively explains this broad temperature range, using physically reasonable parameters. The effect that was lacking in previous models was the very large change with cluster size in the energy per metal atom, measured for the first time by single-crystal adsorption microcalorimetry. Reproducing the broad temperature range in such a heating ramp experiment is equivalent to reproducing very long-term behavior in an isothermal sintering experiment. Although the generalized power law (*6*, *7*, *30*) applies to isothermal sintering experiments, it probably could be made to fit data like those in Fig. 3 by allowing its equilibrium extent of sintering to appropriately increase with temperature. This, however, has no satisfactory atomistic explanation and contradicts the general observation that thermally induced sintering is irreversible upon cooling in vacuum (*8*).

Catalyst sintering kinetics is just one example of many among the various aspects of nanomaterials in which these energetics must have dramatic manifestations. The rate of any process whereby such tiny particles are being either created or consumed must be strongly influenced by these energies, as must estimates of critical cluster sizes in nucleation models. The treatment of sintering by W-J (*3*, *4*) covered a number of other kinetic limits beyond the interface-controlled limit discussed above. Because the factor $e^{\{\mu(R) - \mu(\infty)\}/kT}$ also appears in those rate expressions, it is also crucial to include in them a proper treatment of the dramatic particle size effect on $\mu(R)$ mentioned above. It is equally important to properly treat this dramatic particle size effect on metal atom energy in kinetic models for sintering mechanisms dominated by particle diffusion and agglomeration instead of Ostwald ripening, because the factor $e^{\{\mu(R) - \mu(\infty)\}/kT}$ also appears directly in the rate expression for sintering by that mechanism, at least when particle diffusion requires monomer diffusion around its perimeter (*14*, *15*).

References and Notes

1. M. Valden, X. Lai, D. W. Goodman, *Science* **281**, 1647 (1998).
2. M. Haruta, *Catal. Today* **36**, 153 (1997).
3. P. Wynblatt, N. A. Gjostein, in *Progess in Solid State Chemistry*, J. O. McCaldin, G. A. Somorjai, Eds. (Elsevier Science, Amsterdam, 1975), vol. 9, pp. 21–58.
4. P. Wynblatt, N. A. Gjostein, *Acta Metall.* **24**, 1165 (1976).
5. E. Ruckenstein, D. B. Dadyburjor, *Rev. Chem. Eng.* **1**, 251 (1983).
6. G. A. Fuentes, E. Salinas-Rodriguez, in *Catalyst Deactivation*, C. H. Bartholomew, G. A. Fuentes, Eds. (Elsevier Science, Amsterdam, 1997), pp. 573–583.
7. C. H. Bartholomew, in *Catalyst Deactivation*, C. H. Bartholomew, G. A. Fuentes, Eds. (Elsevier Science, Amsterdam, 1997), pp. 585–592.
8. C. T. Campbell, *Surf. Sci. Rep.* **227**, 1 (1997).

9. T. Bachels, R. Schafer, H. J. Guntherodt, *Phys. Rev. Lett.* **84**, 4890 (2000).
10. L. Q. Yang, A. E. DePristo, *J. Catal.* **149**, 223 (1994).
11. F. Baletto, R. Ferrando, A. Fortunelli, F. Montalenti, C. Mottet, *J. Chem. Phys.* **116**, 3856 (2002).
12. Because the only degrees of freedom of the metal atoms in these clusters are vibrations, the entropic contributions to the free energy are small and differ very little with cluster size. Thus, Eq. 1 is also often applied to describe the size dependence of internal energy as well as free energy. Generally, γ is assumed to be independent of particle radius at the value for bulk metal (*3*, *4*, *13*–*15*).
13. X. Lai, D. W. Goodman, *J. Mol. Catal.* **A162**, 33 (2000).
14. M. J. Jak *et al.*, *Surface Sci.* **474**, 28 (2001).
15. M. J. Jak, C. Konstapel, A. v. Kreuningen, J. Verhoeven, J. W. Frenken, *Surf. Sci.* **457**, 259 (2000).
16. D. E. Starr, D. J. Bald, J. E. Musgrove, J. T. Ranney, C. T. Campbell, *J. Chem. Phys.* **114**, 3752 (2001).
17. The assumption of a constant number density of islands is probably slightly incorrect in that their number generally increases weakly with coverage in this range for such systems (*13*, *41*). Correcting for this would cause the measured decrease in stability with radius to be even more dramatic than shown.
18. W. R. Tyson, W. A. Miller, *Surf. Sci.* **62**, 267 (1977).
19. Using a very new value of γ for Pb [44 μJ/cm^2 (*42*)] gives even poorer agreement with experiment. Using Eq. 1 here neglects the energy of the flat face of the hemisphere, which is equivalent to setting the Pb/MgO adhesion energy at this face equal to the Pb-Pb adhesion energy. [If the Pb/MgO adhesion energy were zero, the factor of 2 in Eq. 1 would instead be 3. In reality, the needed correction is much smaller (*16*).]
20. I. Galanakis, N. Papanikolaou, P. H. Dederichs, *Surf. Sci.* **511**, 1 (2002).
21. R. C. Tolman, *J. Chem. Phys.* **17**, 333 (1949).
22. H. Z. Zhang, R. L. Penn, R. J. Hamers, J. F. Banfield, *J. Phys. Chem. B* **103**, 4656 (1999).
23. D. R. Lide, Ed., *CRC Handbook of Chemistry and Physics* (CRC Press, Boston, MA, ed. 77, 1996).
24. M. Methfessel, D. Hennig, M. Scheffler, *Appl. Phys.* **A55**, 442 (1992).
25. DePristo estimated that relation empirically by extrapolating between measured energies of: the gaseous dimer (CN = 1), a (111) surface (CN = 9), and the bulk (CN = 12). Furthermore, we used DePristo's relation to estimate the errors in the MBA model of Fig. 1 and found that the errors due to the decrease in bond energy with CN nearly compensate for the errors associated with extrapolating between only the most stable clusters, further justifying its use.
26. G. B. McVicker, R. L. Garten, R. T. Baker, *J. Catal.* **54**, 129 (1978).
27. We simplified the definition of E_{tot} ($= \Delta H_{sub} - E_{ad}^{support} + E_{diff}^{support}$) here slightly from that of W-J in that we neglected any excess activation energy (beyond the uphill reaction energy) associated with a monomer detaching from a metal particle to move onto the support surface, because this is tiny relative to E_{tot}.
28. There is another large error in Eq. 3. In its derivation, W-J expanded the exponential factors such as $e^{[\mu(R) - \mu(\infty)]/kT}$ in Taylor series and neglected all but the first two terms. This is equivalent to assuming that $\mu(R) - \mu(\infty)$ is small compared to kT. Inspection of the heat data in Fig. 1 proves that this is clearly not the case below 1000 K for particles with a radius of a few nanometers.
29. D. E. Starr, C. T. Campbell, *J. Phys. Chem.* **B105**, 3776 (2001).
30. C. E. Stassinos, H. H. Lee, *Chem. Eng. Sci.* **50**, 1337 (1995).
31. C. H. Bartholomew, Ed., *Sintering Kinetics of Supported Metals: Perspectives from a Generalized Power Law Approach*, vol. 88 of *Studies in Surface Science and Catalysis* (Elsevier Science, Amsterdam, Netherlands, 1994).
32. V. Bondzie, S. C. Parker, C. T. Campbell, *Catal. Lett.* **63**, 143 (1999).
33. F. Cosandey, T. E. Madey, *Surf. Rev. Lett.* **8**, 73 (2001).
34. S. C. Parker, A. W. Grant, V. A. Bondzie, C. T. Campbell, *Surf. Sci.* **441**, 10 (1999).
35. H. Graoui, S. Giorgio, C. R. Henry, *Philos. Mag. B* **81**, 1649 (2001).
36. C. T. Campbell, D. E. Starr, *J. Am. Chem. Soc.* **124**, 9212 (2002).
37. The average initial radius of Au clusters grown on TiO_2(110) under similar deposition conditions was estimated by scanning tunneling microscopy (*13*) and high-resolution scanning electron microscopy (*33*) to be about 1 nm. We used a slightly smaller average size because those techniques could have missed the smallest particles.
38. M. Gillet, A. A. Mohammed, K. Masek, E. Gillet, *Thin Solid Films* **374**, 134 (2000).
39. S. C. Parker, thesis, University of Washington, Seattle, WA (2000).
40. S. H. Overbury, P. A. Bertrand, G. A. Somorjai, *Chem. Rev.* **75**, 547 (1975).
41. C. R. Henry, M. Meunier, *Mat. Sci. Eng.* **A217/218**, 239 (1996).
42. C. Bombis, A. Emundts, M. Nowicki, H. P. Bonzel, *Surf. Sci.* **511**, 83 (2002).

43. We thank the U.S. Department of Energy, Office of Basic Energy Sciences, Chemical Sciences Division, for support of this work. D.E.S. thanks NSF and the University of Washington Center for Nanotechnology for an IGERT Fellowship.

14 June 2002; accepted 24 September 2002

Heterogeneous Atmospheric Aerosol Production by Acid-Catalyzed Particle-Phase Reactions

Myoseon Jang,* Nadine M. Czoschke, Sangdon Lee, Richard M. Kamens

According to evidence from our laboratory, acidic surfaces on atmospheric aerosols lead to potentially multifold increases in secondary organic aerosol (SOA) mass. Experimental observations using a multichannel flow reactor, Teflon (polytetrafluoroethylene) film bag batch reactors, and outdoor Teflon-film smog chambers strongly confirm that inorganic acids, such as sulfuric acid, catalyze particle-phase heterogeneous reactions of atmospheric organic carbonyl species. The net result is a large increase in SOA mass and stabilized organic layers as particles age. If acid-catalyzed heterogeneous reactions of SOA products are included in current models, the predicted SOA formation will be much greater and could have a much larger impact on climate forcing effects than we now predict.

Gas-phase reactions of volatile organic compounds (VOCs) associated with photochemical oxidant cycles have been of great interest in predicting ozone (O_3) concentrations and, more recently, SOA formation. SOA has received much attention for a variety of reasons, many of which are associated with the establishment of a national ambient air quality standard for atmospheric fine particles (*1*). From a public health perspective, SOAs, which are a major contributor to fine particulate matter, have potentially negative health effects. In particular, it is now believed that the potency of a mixture of environmental chemicals, such as an organic and inorganic multicomponent SOA, may be greater than its constitutive parts (*1*). At the regional scale, SOA formation can contribute to the formation of visibility-reducing haze (*2*). SOAs affect the Earth's radiative balance (*3*, *4*) directly by altering the scattering properties of the atmosphere and indirectly by changing cloud properties. These climate forcing effects are thought to lead to a net cooling effect at the tropospheric level (*3*). Furthermore, the composition of SOAs influences the extent of these effects. For example, the water content of cloud aerosols, and thus a cloud's lifetime, is mainly influenced by particle acidity and sulfate content.

Our understanding of the role SOAs play in climate change and their connection to health effects is limited by numerous uncertainties, particularly the total SOA particle concentration and mass, the contribution of tropospheric SOAs to the total particle load, the composition and physical structure of atmospheric aerosols, and the heterogeneous chemistry that influences these parameters. What is known is that biogenic terpenes from terrestrial vegetation (*5*) and aromatics from anthropogenic sources (*6*) are SOA precursors. Also, the gas-phase photooxidation reaction of these VOCs generates large amounts of multifunctional organic carbonyls (*7*–*10*), which are major SOA components. In addition, these components may react heterogeneously to form an additional generation of products in the particle phase.

A major class of these heterogeneous reactions is the acid-catalyzed reactions of atmospheric carbonyls (*10*, *11*). Principal candidates for atmospheric acid catalysts are sulfuric acid (H_2SO_4) and nitric acid (HNO_3), which are produced through oxidation processing of SO_2 and NO_x emitted from fossil fuel combustion (*12*–*15*). These are inorganic acids; thus, the effects of acid-catalyzed heterogeneous reactions are essentially interac-

Department of Environmental Sciences and Engineering, CB 7431, Rosenau Hall, University of North Carolina at Chapel Hill, Chapel Hill, NC 27599, USA.

*To whom correspondence should be addressed. E-mail: mjang@email.unc.edu